Ultrafast polarization switching in $BaTiO_3$ by photoactivation of its ferroelectric and central modes

Fangyuan Gu [1,*] and Paul Tangney [2]

[1]*Tsung-Dao Lee Institute and School of Physics and Astronomy, Shanghai Jiao Tong University, Shanghai 201210, China*

[2]*Department of Physics and Department of Materials, Imperial College London, London SW7 2AZ, United Kingdom*

(Received 5 December 2023; accepted 1 July 2024; published 16 July 2024)

We use molecular dynamics simulations with machine-learned atomistic force fields to simulate photoexcitation of $BaTiO_3$ by a femtosecond laser pulse whose photon energy exceeds the optical gap. We demonstrate selective displacive excitation of coherent zone-center ferroelectric mode phonons and of the strongly anharmonic central mode. We show that the direction of **P** can either be reversed by a pulse in hundreds of femtoseconds or, on a longer timescale and when combined with a weak field, switched to any one of its symmetry-equivalent directions.

DOI: 10.1103/PhysRevB.110.014307

I. INTRODUCTION

The demand for faster and more efficient optoelectronic devices has motivated a lot of research into the use of femtosecond (fs) laser pulses to quickly change the directions of polarization (**P**) domains in ferroelectric perovskites. Many pulse-based mechanisms of manipulating **P** have been proposed [1–14], but none of them are ready for widespread use in devices. They tend either to use terahertz (THz)-frequency pulses, which couple strongly and directly to optical phonons [3–6] or domain walls [7–9,15,16]; or they use optical pulses, which excite phonons by impulsive stimulated Raman scattering (ISRS) [17–19]. A disadvantage of THz radiation is that the forces it exerts change direction every half period. Therefore using it to permanently switch **P** entails carefully shaping, polarizing and/or coordinating THz pulses [3,5–7,20]. A disadvantage of ISRS is that it involves high-intensity pulses, which can damage a ferroelectric material [3,17,21].

$BaTiO_3$ is a widely used and intensively studied ferroelectric material, which is often regarded as a prototypical ferroelastoelectric perovskite. Therefore understanding its interaction with ultrashort laser pulses is both fundamentally interesting and of practical importance to device design and innovation.

In this work, we present the results of atomistic molecular dynamics (MD) simulations which show that above-optical-gap ($>E_g$) photoexcitation of $BaTiO_3$ with femtosecond (fs) laser pulses would deterministically reverse the direction of **P** within hundreds of fs by a mechanism known as *displacive excitation of coherent phonons* (DECP) [22–28]; while higher intensity pulses would induce a temporary displacive transition to the unpolarized cubic $Pm\bar{3}m$ structure of $BaTiO_3$'s paraelectric phase. The $Pm\bar{3}m$ structure would spontaneously polarize again, via a quasi-random process of domain nucleation and growth [29], when the photoexcited carriers recombined or dispersed. By biasing this process with an applied field or GHz/THz pulses, **P** could be manipulated into any one of its symmetry-equivalent directions.

Although $>E_g$ photons produce a lot of heat in pure $BaTiO_3$ [19,30], there are various ways to mitigate or resolve this problem, such as by doping [28] or by using $(Sr,Ba)TiO_3$ or another similar material whose optical gap is smaller. Furthermore, what makes the DECP-based mechanism of controlling **P** particularly promising for device applications is its robustness and versatility: with lower intensity pulses, which produce less heat, it can be used to weaken an existing **P** field temporarily, so that it can be switched more quickly and easily by another mechanism and stimulus.

To simulate the response of a $BaTiO_3$ crystal to the absorption of a fs $>E_g$ pulse we first performed an MD simulation at thermal equilibrium with a force field that describes $BaTiO_3$'s electronic ground state. Then we simulated the absorption event by replacing the ground state force field with one that describes a photoexcited state, before continuing the MD simulation to observe and analyze the crystal's response. This simple procedure entails making the same physical assumptions about relaxation timescales that have been made, and discussed, in many previous works [14,24,26–28,31–33]. The absorption of a fs $>E_g$ pulse can be approximated as an instantaneous change to the state of the electrons, which takes them out of thermal equilibrium with the lattice, and creates two separate thermalized populations of carriers: conduction band electrons and valence band holes. These carriers' densities (x) are equal, initially, and remain approximately constant for several ps after pulse absorption [14,24,26–28,32,33].

Although we neglect the $\lesssim 100$ fs [34–38] taken for the populations of electrons and holes to thermalize, the DECP mechanism by which a fs $>E_g$ pulse interacts with **P** and with the A_1-symmetry ferroelectric mode (FM) phonon does not require this thermalization, or wait for it to happen. It begins as soon as electrons vacate bonding states and occupy antibonding states, because it is driven by the forces on the crystal's sublattices caused by this change of the electron density. Qualitatively, and semiquantitatively, these forces are

*Contact author: fangyuan.gu@sjtu.edu.cn

determined by x and by the characters of the upper valence band states ($\approx$ O-2p admixed with Ti-3d) and lower conduction band states ($\approx$ Ti-3d admixed with O-2p). They are relatively insensitive to how holes and electrons, respectively, are distributed among these states [28].

There are many other mechanisms by which phonons throughout the Brillouin zone can be excited by high energy carriers. The rate at which electron-phonon scattering heats the lattice should be particularly high during the tens of fs [38] that it takes the carrier energy distributions imposed by the laser pulse to relax into quasistationary thermal distributions of electrons near the bottom of the conduction band and of holes near the top of the valence band [36]. By assuming that they reach these states in an instant, we are neglecting these other phonon excitation processes. However, they are thermal processes, which do no more than heat the lattice [36,38].

What sets the DECP mechanism apart from other phonon excitation mechanisms is that it is a nonthermal mechanism. Instead of simply heating the lattice, it excites *spatially coherent* motion along the eigenvectors of *zone center* phonons [22,27]. In other words, it excites rigid relative motion of the crystal's sublattices, which can be observed indirectly by measuring the changes it induces in a crystal's optical constants.

As we explain next, another distinguishing feature of the DECP mechanism is that, after the initial rapid thermalization of photoexcited carriers, the only phonons that it excites directly are those with A_1 symmetry. The A_1 mode that it excites most strongly in $BaTiO_3$ is the FM, which is a modulation of **P** and of the Ti-O bond distance, $d_{\text{Ti-O}}$. As explained in Ref. [28], strong excitation of the FM is a consequence of photoexcitation reducing the magnitudes of the Ti and O ions' charges, and creating carriers that screen their mutual attraction. Weakening the Ti-O attraction changes the equilibrium values of **P** and $d_{\text{Ti-O}}$. Therefore it changes the equilibrium value of the FM mode coordinate.

A. Selective displacive excitation of motion along the A_1 ferroelectric mode eigenvector

In this subsection, we explain why the DECP mechanism selectively excites modes with A_1 symmetry; and why, in $BaTiO_3$, it excites the FM much more strongly than the other A_1 modes.

1. Selective excitation of modes with A_1 symmetry

A phonon mode has A_1 symmetry if and only if the perfect crystal's symmetry is not lowered by slightly moving it from equilibrium along the mode's eigenvector. All A_1 modes are modes at the Brillouin zone's Γ point ($\mathbf{k} = 0$), which means that the motion of the crystal along an A_1 eigenvector is a rigid relative motion of the crystal's sublattices.

Let us assume that the phonon eigenvectors have been chosen to be mutually orthogonal, and let $\{Q^{\text{eq}}_{\mathbf{k}\mu}\}$ denote the set of values of the phonon mode coordinates when the crystal is at mechanical equilibrium. Therefore, when $Q_{\mathbf{k}\mu} = Q^{\text{eq}}_{\mathbf{k}\mu}$, $\forall \mathbf{k}\mu$, the net force $F_{\mathbf{k}\mu} \equiv -\partial U/\partial Q_{\mathbf{k}\mu}$ on every mode coordinate $Q_{\mathbf{k}\mu}$ vanishes, where U denotes the potential energy, and $\mathbf{k}\mu$ labels the mode with wave vector $\mathbf{k}$ and band index μ.

At equilibrium, the reason that forces on A_1 modes are zero differs from the reason that forces on non-A_1 modes are zero, and understanding this difference is crucial to understanding why the DECP mechanism selectively excites A_1 modes. As we now explain, the forces on non-A_1 modes vanish by symmetry, whereas the forces on A_1 modes vanish because competing contributions to them are balanced and cancel one another. Our explanation is easy to adapt from a state of mechanical equilibrium to a state of *thermal* equilibrium. At thermal equilibrium $F_{\mathbf{k}\mu}$ does not vanish, but its time average or expectation value, $\langle F_{\mathbf{k}\mu}\rangle$, vanishes.

If the perfect crystal is moved away from mechanical equilibrium along the eigenvector of zone center mode $\Gamma\mu$, the orthogonality of eigenvectors implies that $Q_{\Gamma\mu}$ is the only mode coordinate that changes. Let us denote the change of potential energy resulting from the change $Q^{\text{eq}}_{\Gamma\mu} \rightarrow Q^{\text{eq}}_{\Gamma\mu} + q$ by $\tilde{U}_{\Gamma\mu}(q) = \tilde{U}^{\text{n-n}}_{\Gamma\mu}(q) + \tilde{U}^{\text{e-n}}_{\Gamma\mu}(q)$, where $\tilde{U}^{\text{n-n}}_{\Gamma\mu}$ is the energy of Coulomb repulsion between nuclei, and $\tilde{U}^{\text{e-n}}_{\Gamma\mu}$ is the energy of Coulomb attraction between electrons and nuclei.

If mode $\Gamma\mu$ does not have A_1 symmetry, the crystal's symmetry is higher at $q = 0$ than it is when $q \neq 0$. Therefore the functions $\tilde{U}_{\Gamma\mu}(q)$, $\tilde{U}^{\text{n-n}}_{\Gamma\mu}(q)$, and $\tilde{U}^{\text{e-n}}_{\Gamma\mu}(q)$ must have inversion symmetry about $q = 0$. It follows that

$$F_{\Gamma\mu}(q) \equiv -\frac{d\tilde{U}_{\Gamma\mu}}{dq} = -\frac{\partial U}{\partial Q_{\Gamma\mu}}\bigg|_{Q^{\text{eq}}_{\Gamma\mu}+q} = -F_{\Gamma\mu}(-q),$$

and that $F^{\text{n-n}}_{\Gamma\mu} \equiv -d\tilde{U}^{\text{n-n}}_{\Gamma\mu}/dq$ and $F^{\text{e-n}}_{\Gamma\mu} \equiv -d\tilde{U}^{\text{e-n}}_{\Gamma\mu}/dq$ are also odd functions of q. Therefore $F^{\text{n-n}}_{\Gamma\mu}(q)$ and $F^{\text{e-n}}_{\Gamma\mu}(q)$ both vanish at $q = 0$, and this is why $F_{\Gamma\mu}(q) = F^{\text{n-n}}_{\Gamma\mu}(q) + F^{\text{e-n}}_{\Gamma\mu}(q)$ vanishes.

Conversely, if mode $\Gamma\mu$ *does* have A_1 symmetry, symmetry is not lowered by q becoming finite. This implies that the functions $\tilde{U}_{\Gamma\mu}(q)$, $\tilde{U}^{\text{n-n}}_{\Gamma\mu}(q)$, and $\tilde{U}^{\text{e-n}}_{\Gamma\mu}(q)$ do not have symmetry about the value $q = 0$, and that $F^{\text{n-n}}_{\Gamma\mu}$ and $F^{\text{e-n}}_{\Gamma\mu}$ do not vanish at equilibrium. Therefore, at equilibrium, $F_{\Gamma\mu}$ does not vanish by symmetry or because $F^{\text{n-n}}_{\Gamma\mu}$ and $F^{\text{e-n}}_{\Gamma\mu}$ both vanish, but because $F^{\text{n-n}}_{\Gamma\mu} = -F^{\text{e-n}}_{\Gamma\mu}$.

This is the property of an A_1 mode that allows it to be excited by the DECP mechanism: An A_1 mode coordinate can vary within a continuous range without changing the perfect crystal's symmetry, and its equilibrium mode coordinate is the value in that range at which $F^{\text{n-n}}_{\Gamma\mu}$ and $F^{\text{e-n}}_{\Gamma\mu}$ are perfectly balanced. It follows that when the electronic state of a perfect crystal is changed by photoexcitation or any stimulus, causing the magnitude of $F^{\text{e-n}}_{\Gamma\mu}$ to change, the balance is disrupted and $F^{\text{e-n}}_{\Gamma\mu}$ and $F^{\text{n-n}}_{\Gamma\mu}$ are no longer equal in magnitude and opposite in direction. Therefore the stimulus changes $Q^{\text{eq}}_{\Gamma\mu}$.

DECP occurs when an fs laser pulse suddenly creates a high density of photoexcited carriers in a crystal that possesses A_1 phonon modes. This changes the crystal's A_1 mode coordinates suddenly, meaning that the crystal's sublattices suddenly have the wrong relative displacements. Therefore they move along the A_1 eigenvectors towards the new A_1 coordinates, which they overshoot and oscillate about [23,24,28]. This oscillation is the displacively excited coherent A_1 phonon.

After the rapid ($\approx$ 10 fs [38]) thermalization of the photoexcited carriers, it is only A_1 modes that are excited significantly by the change in the electronic state, because thermalization implies loss of coherence and only coherent

electronic states have density matrices with finite off-diagonal elements. Therefore carrier thermalization endows the photoexcited electron density, and the electronic contributions ($F^{\text{e-n}}_{\Gamma\mu}$) to the forces [39,40], with the symmetry of the crystal. It follows that $F^{\text{e-n}}_{\Gamma\mu}$ vanishes by symmetry if $\Gamma\mu$ is not an A_1 mode; and that the equilibrium coordinate $Q^{\text{eq}}_{\Gamma\mu}$ only differs from its value before the laser pulse was absorbed if mode $\Gamma\mu$ has A_1 symmetry.

2. *Polar distortions create* A_1 *phonon modes*

$BaTiO_3$ has three ferroelectric (FE) phases, which all possess A_1 modes and have almost identical electronic structures. Each FE phase only differs from the $Pm\bar{3}m$ structure by tiny symmetry-breaking relative displacements of its sublattices, and an accompanying strain. This breaking of inversion symmetry lifts the degeneracy of the four triply degenerate optical modes, $3F_{1u} + 1F_{2u}$, of the $Pm\bar{3}m$ phase.

Specifically, in the lowest temperature rhombohedral phase ($R3m$), which is the phase that we simulated, each F_{1u} mode has split into an A_1 mode and a doubly degenerate E mode ($F_{1u} \rightarrow A_1 + E$); while the F_{2u} mode has split into an A_2 mode and a doubly degenerate E mode ($F_{2u} \rightarrow A_2 + E$). The room temperature tetragonal FE phase ($P4mm$) is very similar. Each F_{1u} mode has split into an A_1 mode and a doubly degenerate E mode ($F_{1u} \rightarrow A_1 + E$); while the F_{2u} mode has split into a B_1 mode and a doubly degenerate E mode ($F_{2u} \rightarrow B_1 + E$). In both of these phases, all three of the A_1 modes are both infrared active and Raman active.

The distortions that lower the symmetry of the $Pm\bar{3}m$ structure also lower the potential energy by $\Delta U \equiv U_{Pm\bar{3}m} - U_{\text{FE}} > 0$, and create a **P** field [28]. By far the largest contributions to both **P** and ΔU come from the *polar distortion* of $Pm\bar{3}m$ along the eigenvector of the ferroelectric phase's A_1 *ferroelectric mode* (FM), which is a countermotion of the Ti and O sublattices along an axis parallel to **P**. The polar distortion makes the Ti-O Coulombic attraction more negative by shortening the Ti-O bond length, and displacements along the other eigenvectors help to accommodate it [28].

In both $R3m$ and $P4mm$, the three optical A_1 modes are known as the FM, the *Axe mode* (AM) [41], and the *Last mode* (LM) [42]. The eigenvectors in $P4mm$ are easier to visualize, and are shown in Fig. 1(d). The only qualitative difference in $R3m$ is that the sublattices displace along one of the ⟨111⟩ axes, instead of along one of the ⟨001⟩ axes, as shown for the FM in Fig. 2. Both the FM and its counterpart in $Pm\bar{3}m$, which does not have A_1 symmetry, are often referred to as the *soft mode* or the *Slater mode* (SM) [43]. We refer to it as the FM when its A_1 symmetry is relevant and as the SM otherwise.

3. *Selective excitation of the ferroelectric mode*

As discussed above, ultrafast $>E_g$ photoexcitation induces motion along every A_1 eigenvector to some degree, but it *selectively* excites motion along the FM eigenvector in the sense that the AM and LM are excited to much lesser degrees. We demonstrate this selectivity in Sec. III, and briefly explain it here. We discuss it in greater detail in Ref. [28].

Roughly speaking, the SM of a given phase can be viewed as an oscillation of $\Delta_{\text{Ti-O}} \equiv d^{Pm\bar{3}m}_{\text{Ti-O}} - d_{\text{Ti-O}} \gtrless 0$, where $d_{\text{Ti-O}}$ and $d^{Pm\bar{3}m}_{\text{Ti-O}}$ are the Ti-O nearest-neighbor distances in the given phase and in $Pm\bar{3}m$, respectively. We choose the origin for the FM mode coordinate, Q_{FM}, to be where the polar distortion vanishes, i.e., in the $Pm\bar{3}m$ phase. Therefore the thermodynamic averages of Q_{FM}, $\Delta_{\text{Ti-O}}$, **P**, and the contribution, $\mathbf{P}_{\text{FM}}$, of the polar distortion along the FM eigenvector to **P**, approximately satisfy

$$\bar{\mathbf{P}}(T,x) \approx \bar{\mathbf{P}}_{\text{FM}}(T,x) \propto \bar{Q}_{\text{FM}}(T,x) \propto \bar{\Delta}_{\text{Ti-O}}(T,x),$$

where the bar over each quantity denotes that it is the thermodynamic average of that quantity.

As discussed in Ref. [28], photoexcited carriers weaken the Ti-O attraction by screening it and by reducing the magnitudes of Ti and O ions' charges. They reduce charges because promoting electrons from predominantly O-2p bonding states to predominantly Ti-3d antibonding states moves some electron density from O to Ti. Therefore DECP excites the FM strongly because $Q_{\text{FM}} \propto \Delta_{\text{Ti-O}}$ is highly sensitive to x. However, the

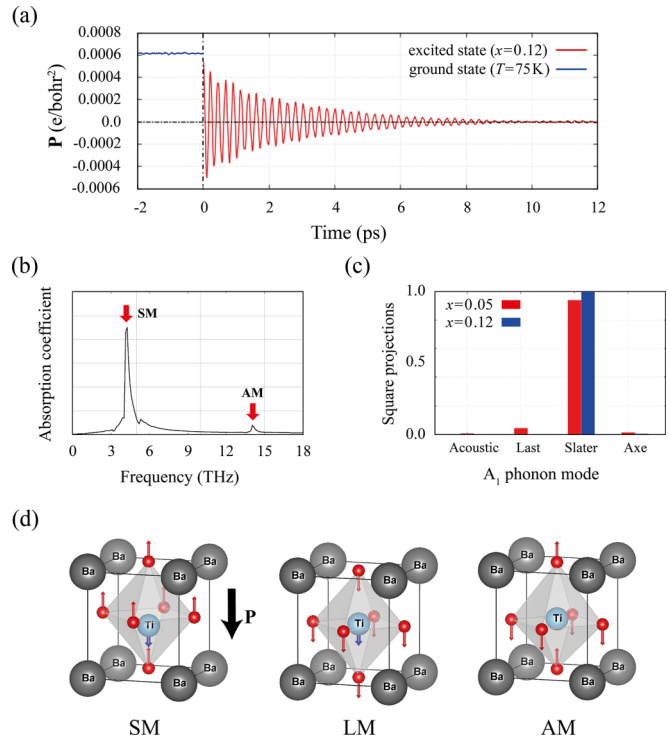

FIG. 1. (a) Polarization **P** as a function of time (t), with $>E_g$ photoexcitation to a carrier density of $x = 0.12\ e^-/\text{f.u.}$ occurring at $t = 0$. (b) The IR absorption spectrum immediately after photoexcitation; (c) Squared projections of the normalized change in the $T = 0$ equilibrium structure, $(\mathbf{R}^{\text{eq}}_x - \mathbf{R}^{\text{eq}}_0)/|\mathbf{R}^{\text{eq}}_x - \mathbf{R}^{\text{eq}}_0|$, onto the three unit-normalized zone-center A_1 optical phonon eigenvectors. At each of the two values of x, the sum of the squared projections is one. (d) The eigenvectors of the three A_1-symmetry zone-center optical modes of $BaTiO_3$'s tetragonal ($P4mm$) phase, which are the *Slater mode* (SM) [43], the *Last mode* (LM) [42], and the *Axe mode* (AM) [41]. Arrows indicate the directions and relative magnitudes of the sublattice displacements. We show eigenvectors in the $P4mm$ phase for clarity. The only qualitative difference in the rhombohedral ($R3m$) phase is that **P** and the sublattice displacements of the SM, LM, and AM eigenvectors are parallel to one of the ⟨111⟩ axes instead of one of the ⟨001⟩ axes.

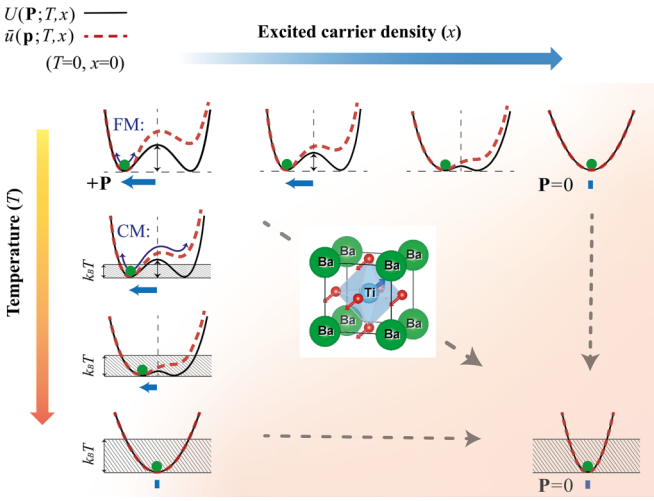

FIG. 2. Schematic illustrating the average potential energy, U and $\bar{u}$, as a function of $\mathbf{P}$ and $\mathbf{p}$, respectively, at $T = 0$ in the electronic ground state and at several finite temperatures (T) and photoexcited carrier densities (x). The $BaTiO_3$ crystal structure in the center illustrates the FM eigenvector of the $R3m$ phase. The Ti-O attraction is responsible for lowering the energy of the $R3m$ structure relative to $Pm\bar{3}m$. This gives U multiple energy minima, corresponding to $R3m$ structures with different $\mathbf{P}$ directions, and a local maximum at $\mathbf{P} = 0$, corresponding to the $Pm\bar{3}m$ structure [28]. The effects on U and $\bar{u}$ of increasing x are similar to the effects of increasing T. They gradually transform into having single minima at $\mathbf{P} = 0$ and $\mathbf{p} = 0$, respectively. This is because carriers weaken the Ti-O attraction by screening it and reducing the magnitudes of ions' charges; while temperature both weakens it and reduces its relevance. Thermal disorder weakens long range electrostatic interactions [44] and increases the average Ti-O distance [45,46], and the potential energy cost of thermal fluctuations grows with increasing T until it dwarfs the Ti-O attraction.

AM and LM do not depend linearly on $\Delta_{\text{Ti-O}}$ and there is no obvious reason why DECP would excite them strongly.

II. SIMULATION METHODS

We performed MD simulations of the $R3m$ phase with three different force fields. One of the force fields was developed and used to describe the crystal before absorption of a laser pulse, and the other two were developed and used to describe it after the absorption of laser pulses of two different intensities, and therefore at two different levels of photoexcitation. We assumed that the crystal was in its electronic ground state ($x = 0$) before pulse absorption, and our photoexcited-state force fields modeled carrier densities of $x = 0.05$ conduction band electrons per $BaTiO_3$ formula unit (e^-/f.u.) and $x = 0.12$ e^-/f.u.

We simulated photoexcitation at various different temperatures T. At each value of T, we performed a long MD simulation with the ground state ($x = 0$) force field to reach thermal equilibrium. Then, at a time that we designated $t = 0$, we simulated pulse absorption by replacing the $x = 0$ force field with one of the two photoexcited state force fields. Then we continued the MD simulation to see how the crystal responded to the photoexcited carriers changing the interactions between ions.

A. Force fields

The parameters of each force field were fit to density functional theory (DFT) calculations of thermally disordered crystals. We fit our ground state force field to ground state DFT calculations, and our photoexcited state force fields to constrained DFT calculations [24,27,28]. All of our DFT and constrained DFT calculations were performed with the PBEsol functional [47].

In constrained DFT calculations, the difference between a photoexcited electronic state and the electronic ground state is modeled by populating the conduction and valence bands with independently thermalized populations of electrons and holes, respectively, with equal densities, x, of conduction band electrons and valence band holes [24,26,27,32]. Our constrained DFT calculations of $BaTiO_3$ are discussed in detail in Ref. [28].

1. Mathematical form

The mathematical form of our force fields is presented in detail in Appendix A. It can be expressed as a sum of interactions between pairs of ions, where the interaction between each pair is the sum of a Morse potential [48] and an electrostatic interaction. Although the electrostatic interaction can be expressed as a sum of *apparently* pairwise terms, each of the terms is really a function of all ions' positions and is therefore a many-body interaction.

The Morse interaction energy between two ions has the form

$$U^{\text{Morse}} = D[1 - \exp(-C(r - r^0))]^2,$$

where C, D, and r^0 are parameters, and r is the distance between them. It only acts at short range and it is repulsive when the ions are very close to one another and attractive when they are slightly farther apart. It is a truly *pairwise* interaction because it does not depend on the positions of any other ions.

The electrostatic energy of interaction between two ions is a sum of contributions from charge-charge, charge-dipole, dipole-charge, and dipole-dipole interactions. However, these are not interactions between *point* charges and *point* dipoles if the two ions are close to one another: When the distance r between two ions is small, the dependence of their interaction on r is adjusted to account for the overlap of their electron clouds.

Furthermore, each ion's dipole moment is not simply $\mathbf{d} = \alpha\mathbf{E}$, where $\mathbf{E}$ is the electric field at the nucleus and α is an isotropic scalar polarizability. It is $\mathbf{d} = \alpha\mathbf{E} + \mathbf{d}_{\text{sr}}$, where $\mathbf{d}_{\text{sr}}$ is a contribution from the distortion of the ion's electron cloud by *overlap repulsion*. When ions are close enough, the electron density between them is not simply a superposition of their electron clouds. If it were, the density of electrons between them would be very high, and so the kinetic energy of the electrons between them would be very high. To reduce their kinetic energy, electrons move out of the space between the two nuclei. This strengthens the Coulomb repulsion between the nuclei, and changes the shape of each

ion's electron cloud. We use $\mathbf{d}_{sr}$ to model the effects on Coulomb interactions of the changes of an ion's shape caused by this overlap repulsion. This is a nonelectrostatic mechanism by which an ion's neighbors help to determine the value of its dipole moment, and influence its interaction with all other ions.

Even if the force field did not describe the effects of ions' electron clouds overlapping, and distorting one another via their mutual repulsion, the electrostatic interaction between two ions would not be pairwise because each ion's dipole moment **d** is determined by the local electric field **E**, and **E** is determined by the positions, charges, and dipole moments of all of the other ions. Therefore the electrostatic interaction between two ions depends on the positions of *all* ions.

2. *Variable charges versus fixed charges*

As discussed in Ref. [28] and in many other works (e.g., Refs. [49,50]), the lower conduction bands and the upper valence bands of $BaTiO_3$ are all hybrid states: they are linear combinations of both O-2p and Ti-3d atomic orbitals. The upper valence bands have roughly 70%–80% O-2p character, and the lower conduction bands have roughly 70%–80% Ti-3d character, but this changes to some degree as ions move, causing the electric potential at each point in space to change. As the potential of each ion changes, it shifts the ion's orbitals up and down in energy, which would cause some degree of variation in the amounts of O-2p and Ti-3d characters of the upper valence bands and lower conduction bands, and therefore some degree of variation of the net charges of O anions and Ti cations.

To model this effect, Sarsam [51] and Nemytov [52] have developed force fields that allow each ion to simultaneously polarize in response to its local electric field [53–56] and vary its charge in response to changes of its local electric potential [57]. They found that allowing ions' charges to vary did not substantially improve the accuracies of polarizable force fields for some insulating simple oxides in their electronic ground states, including $BaTiO_3$. However, electrons in photoexcited states are more delocalized and mobile, and we have found that variable charges significantly improve the ability of our force field to fit the constrained DFT potential energy surface of photoexcited states.

Therefore we parameterized a more accurate set of variable charge (also known as *charge equilibration* or *qEq*) and polarizable ion force fields for the ground and photoexcited states. These force fields are significantly more expensive computationally; and, as explained in Appendix B, they cannot be used to calculate infrared spectra. Therefore the results that we present in Figs. 1, 3, 5, and 6 are from MD simulations with fixed charge force fields. However, we used our variable charge force fields to check that greater accuracy did not alter the response of **P** to photoexcitation qualitatively, and that the quantitative changes were slight.

In Ref. [58] (see also Refs. [59–63]), we present the results of tests of our force fields and we provide their parameters.

3. *Parameterization protocol*

Our parametrization protocol is discussed in detail in Refs. [51,52,54,55,64]. Briefly, to construct each force field we performed several (≈ 5) parametrizations in order to achieve consistency between the microstructures to which the parameters were fit and the microstructures that those parameters subsequently produced in MD simulations. Iterating parameter sets until self-consistency of microstructures is achieved greatly improves the accuracies and transferabilities of force fields, such as ours, that are fit to effectively infinite *ab initio* data sets [54,64,65].

Achieving self-consistency is particularly important if the microstructures used to calculate DFT data sets are generated by force field-based MD simulations: Regardless

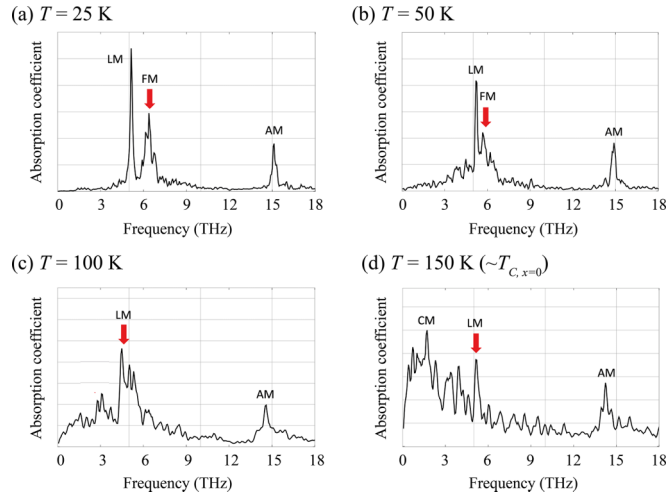

FIG. 3. Infrared absorption spectra in the electronic ground state at different temperatures.

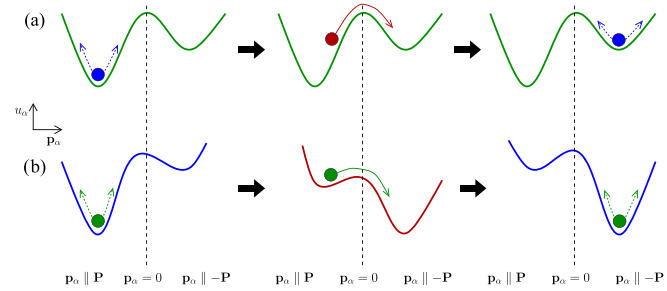

FIG. 4. Schematic illustrating two limits of the complex mechanism by which thermal fluctuations change the direction of the dipole moment per unit volume $\mathbf{p}_\alpha$ of the αth unit cell. Each limit is depicted as a sequence of three curves, representing one-dimensional versions of the local potential energy surface (PES), $u_\alpha(\mathbf{p}_\alpha)$, on which $\mathbf{p}_\alpha$ moves. If long range interactions dominate, as depicted in (a), the PES is dominated by the term $-\mathbf{p}_\alpha \cdot \mathbf{P}$, and is approximately time invariant. $\mathbf{p}_\alpha$ spends most of its time oscillating about the deeper $\mathbf{p}_\alpha \parallel \mathbf{P}$ minimum, but occasional large thermal fluctuations, whose frequency increases with temperature, bring it into the $\mathbf{p} \parallel -\mathbf{P}$ minimum. While there, it slightly reduces the magnitude of **P**, because **P** is the average of $\mathbf{p}_\alpha$ over all primitive cells α. However, it returns to the $\mathbf{p} \parallel \mathbf{P}$ minimum relatively quickly because the barrier it must surmount to return is smaller. In (b), the PES is strongly time dependent because short range interactions dominate. The instantaneous shape of $u_\alpha(\mathbf{p}_\alpha)$ is determined by the strains and dipole moments of neighboring cells, and $\mathbf{p}_\alpha$ simply follows the position of the deeper minimum as it moves between the two directions.

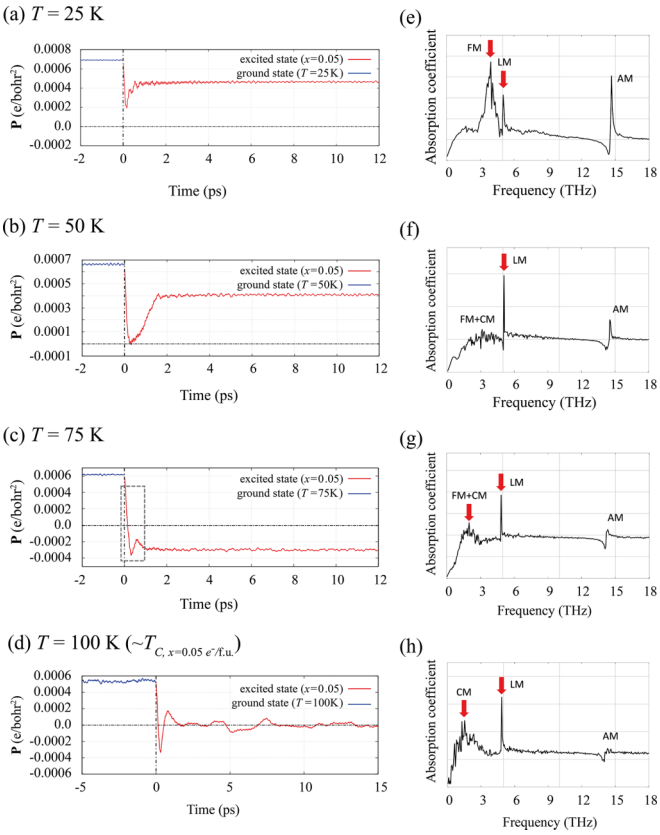

FIG. 5. [(a)–(d)] **P** as a function of time in NVE simulations of ultrafast photoexcitation to a carrier density of $x = 0.05\ e^-/\text{f.u.}$ at four temperatures. [(e)–(h)] IR absorption spectra at the same four temperatures immediately after the simulated pulse absorption at $t = 0$.

of the quantity of data that parameters are fit to, if only one parametrization is performed, the fit to the data used in the parametrization is invariably much better than the fit to *ab initio* data that was not used in the parametrization [65]. However, even when *ab initio* MD is used to generate the initial data set, it can be important to perform further parametrizations in which the data from *ab initio* MD is supplemented with data calculated from microstructures generated by the force field [66].

At each iteration of our self-consistent parametrization procedure we fit the force field's parameters to the forces, stress tensors, and energy differences of ≈ 20–30 microstructures at temperatures of 100, 200, 300, and 500 K. Each microstructure was a set of atomic positions taken from a long MD simulation of a $3 \times 3 \times 3$ supercell (135 atoms) performed with the parameter set produced by the previous iteration. Therefore, at each iteration we fit the 30 (fixed charge) or 39 (variable charge) parameters of the force field to a different set of $N_{\text{data}} \sim 10^4$ numbers, and iterated until the closeness of the fit achieved during parametrization was matched by the closeness of the fit to approximately N_{data} data which had not been used in the parametrization [58].

B. Molecular dynamics simulations of pulse absorption

We used a $12 \times 12 \times 12$ supercell (8640 atoms), under periodic boundary conditions, and performed long MD simulations with the $x = 0$ potential to equilibrate, before modeling fs $>E_g$ pulse absorption by switching abruptly to one of the photoexcited potentials. We calculated the **P** autocorrelation function, $\langle \mathbf{P}(t_0)\mathbf{P}(t_0 + t)\rangle_{t_0}$, from the first 10 ps after photoexcitation and Fourier transformed it to calculate the infrared (IR) absorption spectrum, as described in Appendix B.

Both ΔU and the ferroelectric to paraelectric transition temperature, T_C, are highly sensitive to strain and are lowered by compression [67]. Therefore, when force fields or DFT overestimate the density, it is common to perform calculations at the experimental density or under negative pressure [45,68]. We found $T_C \approx 150$, ≈ 100, and ≈50 K for our $x = 0$, 0.05, and $0.12\ e^-/\text{f.u.}$ force fields, respectively. However, we chose not to apply negative pressure because working at a low T allowed us to observe the DECP mechanism with less thermal noise, and to calculate spectra with signal-to-noise ratios closer to those that would be obtained with simulation cells comparable in size to the photoexcited regions in pump-probe experiments.

III. RESULTS

Figure 1(a) is a plot of **P** as function of time (t) in MD simulations of photoexcitation to a carrier density of $x = 0.12\ e^-/\text{f.u.}$ at $T = 75$ K. At $t = 0$, photoexcitation changes the value of **P** at thermal equilibrium from $\bar{\mathbf{P}}(75\text{ K}, 0) \approx 6 \times 10^{-4}\ e^-/\text{bohr}$ to $\bar{\mathbf{P}}(75\text{ K}, 0.12\ e^-/\text{f.u.}) = 0$. The latter vanishes because $Pm\bar{3}m$ is the thermodynamically stable phase at $(T, x) = (75\text{ K}, 0.12\ e^-/\text{f.u.})$ with our force field. Therefore the fs pulse causes $\bar{\mathbf{P}}$ to vanish suddenly as a consequence of $\bar{Q}_{\text{FM}}$ and $\bar{\Delta}_{\text{Ti-O}}$ vanishing suddenly.

The change of $\bar{Q}_{\text{FM}}$ excites a large amplitude SM phonon by displacively exciting motion along the FM eigenvector. This manifests in Fig. 1 as a damped oscillation of **P** about $\mathbf{P} = 0$, with an initial amplitude of $|\bar{\mathbf{P}}(75\text{ K}, 0)|$. Figure 1(b) is the IR absorption spectrum calculated immediately after photoexcitation to a carrier density of $x = 0.12\ e^-/\text{f.u.}$. The very high intensity of the SM demonstrates that it is excited much more strongly by photoexcitation than any other mode. In Fig. 1(c), for each of our two finite values of x, we plot the squared projections of $(\mathbf{R}_x^{\text{eq}} - \mathbf{R}_0^{\text{eq}})/|\mathbf{R}_x^{\text{eq}} - \mathbf{R}_0^{\text{eq}}|$ onto the unit-normalized A_1 eigenvectors of the photoexcited crystal, where the vectors $\mathbf{R}_0^{\text{eq}}$ and $\mathbf{R}_x^{\text{eq}}$ specify the crystal's $T = 0$ equilibrium structure (the $\sqrt{\text{mass}}$-weighted positions of the atoms) in the electronic ground state and in the photoexcited state, respectively. The fact that the sums of these squared projections are both one demonstrates that the only modes whose eigenvectors are changed by photoexcitation, and therefore which are displacively excited, are those with A_1 symmetry. The fact that the squared projection onto the SM/FM eigenvector is much larger than the squared projections onto the other modes demonstrates that DECP selectively excites this mode.

To better understand what happens when a fs $>E_g$ pulse is absorbed, it is useful to regard the FM as an oscillation of **P**. If $\mathbf{p}_\alpha$ denotes the dipole moment of the αth primitive cell of the crystal divided by its volume, then **P** is the average of $\mathbf{p}_\alpha$ over all cells α; and $\bar{\mathbf{P}}(T, x)$ is the value shared by **P** and the time average of each $\mathbf{p}_\alpha(t)$ at thermal equilibrium. Therefore a displacively excited FM phonon can be viewed as a

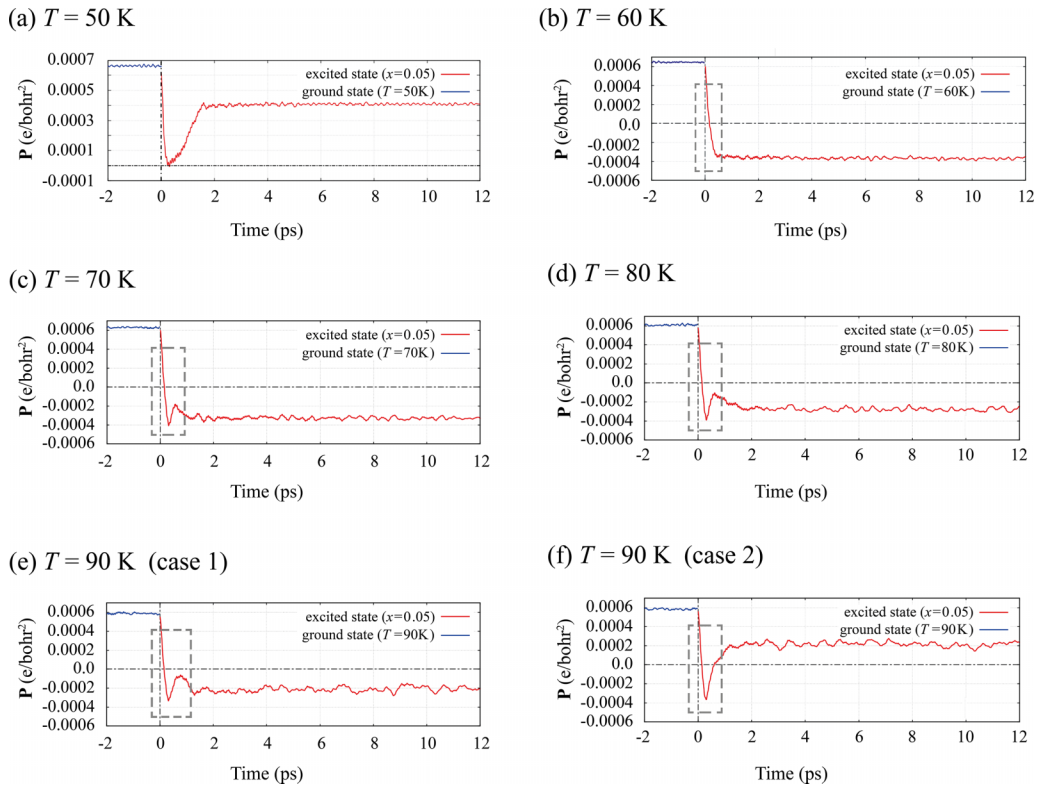

FIG. 6. **P** as a function of time in NVE simulations of ultrafast photoexcitation to a carrier density of $x = 0.05\ e^-/\text{f.u.}$ at five temperatures. When simulations were repeated five times at each temperature, deterministic behavior was found at most temperatures: either **P** did not reverse in every simulation, or it reversed and returned to its original direction, or it reversed and remained reversed, or it reversed but then settled at the value $\mathbf{P} = 0$. However, as plots (e) and (f) illustrate, close to the critical temperature $T_{C,x=0.05\ e^-/\text{f.u.}} = 100$ K, above which **P** vanishes, the behavior of **P** was statistical. This is likely to be a consequence of the small size of our simulation cell, and is unlikely to be relevant to experiments or device applications.

collective motion of the set $\{\mathbf{p}_\alpha\}$ of all **p**'s, which is caused by a sudden change of $\bar{\mathbf{P}}$ from $\bar{\mathbf{P}}(T, 0)$ to $\bar{\mathbf{P}}(T, x)$, and which has an initial amplitude of $\Delta\bar{\mathbf{P}}(T, x) \equiv |\bar{\mathbf{P}}(T, 0) - \bar{\mathbf{P}}(T, x)|$. The motion is collective in the statistical sense that the *average* time derivative of the **p**'s is finite, and remains finite until the crystal reaches a new thermal equilibrium in which the time averages of the **p**'s are all equal to $\bar{\mathbf{P}}(T, x)$.

Now consider a simple model of the crystal in which $\mathbf{p}_\alpha$ completely specifies the structure of the αth cell, and in which $\bar{\mathbf{P}} = \bar{\mathbf{P}}_{\text{FM}}$. Our only reason for representing the structure of each cell by its dipole moment is to make it easier to discuss interactions between cells and correlations between their structures. We are not approximating interactions between cells as dipole-dipole interactions, or making any other strong assumptions about interactions. We are simply assuming that the contribution of each cell to the potential energy of the crystal is determined by how closely its structure is aligned with the structures of other cells. Then we are assuming that, for the purpose of *discussing* interactions and correlations, all relevant aspects of the structure of cell α, such as its strain, are correlated strongly enough with $\mathbf{p}_\alpha$ that they can be represented by $\mathbf{p}_\alpha$.

Therefore let $u_\alpha(\mathbf{p}_\alpha; T, x, t)$ denote the potential energy *of the entire crystal* as a function of $\mathbf{p}_\alpha$ when all other **p**'s are fixed at their instantaneous values at time t; and let $\bar{u}(\mathbf{p}; T, x)$ denote the average of u_α over all α or over time.

Each u_α is time dependent because it is highly sensitive to the structures and strains of surrounding cells [45]. Instantaneously, it is not symmetric about $\mathbf{p}_\alpha = 0$, and it may be a single well or an asymmetric double well, with the (deeper) minimum continuously moving as the **p**'s of surrounding cells change [45]. $\bar{u}(\mathbf{p}; T, x)$ is also asymmetric because, on average, the off-center displacement of the deepest minimum of u_α must be parallel to **P**. However, it is time independent because it is a thermodynamic average.

Now let $U(\mathbf{P}; T, x)$ denote the thermodynamic average of the potential energy over all microstates of the crystal for which $\mathbf{P}_{\text{FM}} = \mathbf{P}$. U is time independent because it is a thermodynamic average, and it has the symmetry of the crystal because, as long as the average magnitude of the **p**'s does not change, the crystal's energy is not changed by switching their average direction to any one of the eight symmetry-equivalent polarization directions of the $R3m$ structure.

Figure 2 shows schematic cross sections of U and $\bar{u}$ along the axis passing through $\bar{\mathbf{P}}_{\text{FM}}$ and $-\bar{\mathbf{P}}_{\text{FM}}$ as both T and x are varied. When $(T, x) \approx (0, 0)$, U is a symmetric double well, with the wells at $\mathbf{P} = \pm\bar{\mathbf{P}}_{\text{FM}}(T, x)$ corresponding to symmetry-equivalent $R3m$ structures. The energy barrier separating them is at $\mathbf{P} = 0$, which corresponds to the $Pm\bar{3}m$ structure within this simple model, and its height is $\Delta U(T, x) \equiv U(0; T, x) - U(\bar{\mathbf{P}}_{\text{FM}}(T, x); T, x)$.

The zone-center FM is a coherent collective oscillation of the $\mathbf{p}$'s about $\mathbf{p} = \bar{\mathbf{P}}_{\mathrm{FM}}$. Both experimentally [69,70], and in our $x = 0$ simulations (Fig. 3), increasing T causes the FM's IR absorption peak to soften and broaden, and a very broad peak, known as the *central mode* (CM), to emerge in the frequency range of 0–3 THz. The CM is not one of the crystal's normal modes, and it does not exist in the $T \to 0$ limit. It gradually becomes active as T increases and the directions of the $\mathbf{p}$'s become disordered. It is common to view the dynamics of each $\mathbf{p}_\alpha$ as motion on a potential energy surface with eight minima [28,71–73]. At each minimum, $\mathbf{p}_\alpha$ is parallel to the displacement of a different one of the eight Ba atoms at the corners of the cell shown in Fig. 2, from the center of that cell [74–76]. The CM is often thought of as a collective hopping motion of the $\mathbf{p}$'s between two or more of these eight minima. However, Fallon's calculations of u_α for various structures of surrounding cells (Ref. [45], Sec. 7.4) suggest that it may be more realistic to view $\mathbf{p}_\alpha$ as moving on a continuously changing surface with only one minimum. Therefore, instead of $\mathbf{p}_\alpha$ hopping between eight ever-present minima of a relatively passive potential energy surface, it might simply follow a single minimum around as it is moved by the rapidly changing $\mathbf{p}$'s of surrounding cells. These two limiting cases are illustrated in Fig. 4.

Figure 4(a) illustrates how thermal fluctuations switch the direction of $\mathbf{p}_\alpha$ in the limit in which long range order is a consequence of long range interactions. This is the limit in which the energy of $\mathbf{p}_\alpha$ is dominated by its coupling to the macroscopic field $\mathbf{P}$ and $u_\alpha(\mathbf{p}_\alpha) \propto -\mathbf{p}_\alpha \cdot \mathbf{P}$ is a good approximation. Since $\mathbf{P}$ is the average of $\mathbf{p}_\alpha$ over all cells, it is a thermodynamic quantity and approximately independent of time, which means that u_α is approximately independent of time. Therefore Fig. 4(a) illustrates the limit in which $\mathbf{p}_\alpha$ moves on an approximately static, but temperature dependent, potential energy surface.

The opposite limit, which is more consistent with Fallon's results, is illustrated by Fig. 4(b). In this limit, the coupling of $\mathbf{p}_\alpha$ to $\mathbf{P}$ makes a negligible contribution to u_α. Instead, long range order emerges from local ordering caused by the short range interactions of each cell with the cells in its immediate surroundings. Senn *et al.* demonstrated that long range order can emerge from short range interactions in Ref. [72].

Regardless of how active a role the time dependence of u_α plays, the CM peak is the spectral signature of the relatively slow and anharmonic large-amplitude "rattling" of the $\mathbf{p}$'s between multiple directions, which emerges as they gain enough thermal energy to change direction. At low T, when most $\mathbf{p}$'s are aligned, $\mathbf{p}_\alpha$ spends most of its time near the $\mathbf{p}_\alpha \parallel \mathbf{P}$ site. As T increases it spends an increasing fraction of its time at the other seven sites. Therefore the directional disorder of the $\mathbf{p}$'s reduces $|\bar{\mathbf{P}}|$ and $|\bar{\mathbf{P}}_{\mathrm{FM}}|$ and, if short range interactions dominate energetics, as depicted in Fig. 4(b), it makes $\bar{u}$ more symmetric because the minimum of u_α spends more of its time at the $\mathbf{p}_\alpha \parallel (-\mathbf{P})$ site.

Disorder also reduces ΔU because the potential energy is lower when each $\mathbf{p}$ is parallel to its neighbors. Reducing $\Delta U/(k_B T)$ increases the proportion of time for which the direction of each $\mathbf{p}$ differs significantly from that of $\mathbf{P}$, and reduces the fraction of the $\mathbf{p}$'s that, at any given time, are participating in the FM, i.e., performing small synchronized oscillations about energy minima at their $\mathbf{p} \parallel \mathbf{P}$ sites. Therefore, when the CM becomes active it amplifies itself by generating disorder that makes it easier for the $\mathbf{p}$'s to change direction.

The FM IR absorption peak shrinks as the CM peak grows with increasing T because, as more $\mathbf{p}$'s contribute to the CM, fewer are available to participate in it. It also softens and broadens because reducing ΔU makes the wells in U shallower, which reduces their curvatures and makes them less harmonic. As T increases even further, the $\mathbf{p}$'s become so disordered that ΔU vanishes and U becomes a single well with a minimum at $\mathbf{P} = 0$. At the lowest values of T for which $Pm\bar{3}m$ is stable, U is approximately quartic (i.e., flat-bottomed; see Fig. 2), meaning that a sufficiently small polar distortion neither raises nor lowers U. When T is larger, U is quadratic near its minimum and its curvature increases as T increases [28].

As discussed in Ref. [28], and the caption of Fig. 2, the effects on $\bar{u}$ and U of increasing x are similar to the effects of increasing T: by weakening the Ti-O attraction, photoexcited carriers reduce both ΔU and the magnitude of the polar distortion [28]. Therefore increasing x reduces $\bar{\mathbf{P}}_{\mathrm{FM}}$ by moving the two minima of U closer together and, by making the two energy wells shallower [28], it lowers the FM frequency, makes it less harmonic, and makes the CM more active. Therefore it decreases the proportion of time for which each $\mathbf{p}$ is approximately parallel to $\mathbf{P}$.

There is no CM peak in Fig. 1(b) because, at $(T, x) = (75\ \mathrm{K}, 0.12\ e^-/\mathrm{f.u.})$, the combined effects of x and T make U a single approximately quadratic well. Instead of the $\mathbf{p}$'s rattling between different directions with very large amplitudes, as they would at lower values of x or T, their collective motion is a superposition of the $Pm\bar{3}m$ phase's three degenerate SMs. When x is large or $T - T_C$ is large and positive, each zone-center SM of $Pm\bar{3}m$ is an oscillation of one of three mutually orthogonal components of $\mathbf{P}$ about the approximately quadratic minimum (at $\mathbf{P} = 0$) of a function identical to $U(\mathbf{P}; T, x)$. When x and/or T are either very large or very small, the CM is not active, the minima of U and $\bar{u}$ have relatively high curvatures, and thermal fluctuations of the $\mathbf{p}$'s are much smaller than when the CM is active. Figures 5(a)–5(d) are plots of $\mathbf{P}(t)$ in simulations of photoexcitation to a much smaller carrier density ($x = 0.05\ e^-/\mathrm{f.u.}$) than in the simulations reported in Fig. 1 ($x = 0.12\ e^-/\mathrm{f.u.}$). $R3m$ is stable at $(T, x) = (75\ \mathrm{K}, 0.05\ e^-/\mathrm{f.u.})$, while $Pm\bar{3}m$ is stable at $(T, x) = (100\ \mathrm{K}, 0.05\ e^-/\mathrm{f.u.})$. The IR spectra in Figs. 5(e)–5(h) show the emergence of the CM as T increases, and that the FM has softened before its peak disappears. They also show that, at $T = 100$ K, the CM still has a substantial peak. This implies that the oscillation of $\mathbf{P}$ about $\mathbf{P} = 0$ in Fig. 5(d) is not simply a superposition of small-amplitude harmonic SMs. It implies that the average magnitude of the $\mathbf{p}$'s is large, that the $\mathbf{p}$'s are disordered, that each $\mathbf{p}$ is rattling between multiple directions with a large amplitude, and that U and $\bar{u}$ are either flat, or shallow double wells. This explains why the oscillations about $\mathbf{P} = 0$ in Fig. 5(d) are so much less harmonic than those in Fig. 1(a), and why, when $T \leqslant 75$ K, the damping of the displacively excited motion along the FM eigenvector is strong enough for $\mathbf{P}$ to stabilize at $\mathbf{P} \approx \bar{\mathbf{P}}(T, 0.05\ e^-/\mathrm{f.u.})$ almost immediately.

The damping of the collective component of the motion of the **p**'s can be viewed as their motions falling out of synchronicity. It is a crucial ingredient in the pulse-induced **P**-reversal mechanism that we propose, and which Fig. 5(c) demonstrates. Without it, **P** would return to its original direction almost as quickly as it reversed. However, Fig. 5(c) demonstrates that **P** reverses in less than half a FM period and remains reversed. The motion of **P** is the collective component of the motion of the **p**'s. Therefore this demonstrates that the collective motion of the **p**'s is so dissipative that, after its direction reverses, it does not have enough energy to return **P** to its original direction.

To investigate whether, or to what degree, **P** reversal is deterministic, we performed five independent simulations at each of the six temperatures, 50, 60, 70, 80, 90, and 100 K. The results of some of these simulations are presented in Fig. 6. At all temperatures except $T = 90$ K the same qualitative behavior of **P** was observed in all five simulations. Therefore, at least at most temperatures, the **P** reversal mechanism that we demonstrate is deterministic. However, when the temperature is approaching the critical value $T_{C,x=0.05\ e^-/\text{f.u.}} = 100$ K, the behavior in our simulations was not deterministic, as illustrated by the results of the two simulations at $(T, x) = (90\text{ K}, 0.05\ e^-/\text{f.u.})$ plotted in Figs. 6(e) and 6(f). Out of our five simulations at 90 K, **P** reversed and returned back to its original direction in two simulations and reversed permanently in the other three.

It is important to note, however, that the degree to which this **P** reversal mechanism is statistical rather than deterministic would be much less in a device or a pump-probe experiment than it is in our simulations of only 1728 unit cells. Furthermore, the range of temperatures for which **P** reversal is deterministic depends on the value of x. Therefore there must exist a wide range of temperatures at which deterministic **P** reversal is possible with an appropriate choice of pulse fluence.

IV. SUMMARY

We have used MD simulations to show that a femtosecond $>E_g$ pulse would selectively excite relative motion of a $BaTiO_3$ crystal's sublattices along the eigenvector of its A_1-symmetry ferroelectric mode, and reduce both the coercive field strength (E_c) and the magnitude of $\bar{\mathbf{P}}$.

Our simulations demonstrate that, for a T-dependent range of pulse fluences, the pulse-induced motion along the FM eigenvector would reverse **P** within 100's of fs without subsequently returning it to its original direction; and that, at higher fluences, the pulse would induce a transient transition to the paraelectric $Pm\bar{3}m$ phase.

Although pulse-induced reversal of **P** is permanent in certain fluence and/or temperature ranges, the reductions of E_c and $|\bar{\mathbf{P}}|$, and the photoinduced stability of $Pm\bar{3}m$ [Figs. 1(a) and 5(d)] would only last until x is reduced by electron-hole recombination and/or diffusion. During the lifetime of the photoexcited state, which might be as short as tens of ps or as long as many nanoseconds [34], the ultimate direction of **P** could be determined by a weak bias, such as an applied field, or by a different pulse-induced mechanism [4,6,13,77]. Therefore a slower method of manipulating **P**, but one capable of placing it into any of its symmetry-equivalent directions, would be to bias the process by which the transient paraelectric phase spontaneously repolarizes when electrons return to their ground state.

Our simulations also suggest that much could be learned about $BaTiO_3$ and related materials from pump-probe experiments that exploit the DECP mechanism to selectively excite the soft mode.

ACKNOWLEDGMENTS

We acknowledge helpful discussions with Éamonn Murray, Wei Ku, Wei Wang, Chi-Ming Yim, Zefang Lv, Jie Chen, and Gabriele Coiana. We also acknowledge financial support from the International Postdoctoral Exchange Fellowship Program (YJ20210137) by the Office of China Postdoc Council (OCPC).

APPENDIX A: MATHEMATICAL FORM OF THE FORCE FIELDS

Each of our force fields is defined by a set of parameters, $\boldsymbol{\eta}$, and by the mathematical form of the potential energy function of atomic positions, $U(\{\mathbf{r}_i\})$. The general form of the potential energy function is $U = U^{\text{Morse}} + U^{\text{elect}} + U^{\text{self}}$, where $U^{\text{Morse}} \equiv \sum_{i,j>i} U_{ij}^{\text{Morse}}$ is a pairwise Morse potential to describe nonelectrostatic short-range interactions between ions; $U^{\text{elect}} \equiv \sum_{i,j>i} U_{ij}^{\text{elect}}$ describes both long range electrostatic interactions and electrostatic interactions between overlapping ions; and $U^{\text{self}} \equiv \sum_i U_i^{\text{self}}$, which we explain below, is the sum of the ions' *self-energies*.

The Morse interaction between ions i and j has the form

$$U_{ij}^{\text{Morse}} \equiv D_{s_i s_j}\left[e^{\gamma_{s_i s_j}\left(1-\frac{r_{ij}}{r^0_{s_i s_j}}\right)} - 2e^{\frac{1}{2}\gamma_{s_i s_j}\left(1-\frac{r_{ij}}{r^0_{s_i s_j}}\right)}\right],$$

where $s_i \in \{\text{Ba, Ti, O}\}$ denotes the species of ion i, $r_{ij} \equiv |\mathbf{r}_i - \mathbf{r}_j|$ is the distance between ions i and j, and $D_{s_i s_j}, \gamma_{s_i s_j}, r^0_{s_i s_j} \in \boldsymbol{\eta}$ are among parameters that we fit. If $C \equiv \gamma/r^0$, the expression for U^{Morse} quoted in Sec. II only differs from this one by an irrelevant additive constant. The Morse potential was not chosen for physical reasons but because, for several oxides, we have found that it allows a closer fit to DFT data to be achieved than can be achieved with other mathematical forms, such as sums of inverse powers of r_{ij} [53–56].

The electrostatic interaction between ions i and j is

$$U_{ij}^{\text{elect}} = \overbrace{\kappa q_i q_j\left(\frac{1}{r_{ij}} - w_{qq}\tilde{I}_{s_i s_j}(r_{ij})\right)}^{\text{charge-charge}} + \overbrace{\kappa\sum_\alpha\left(d_i^\alpha q_j - q_i d_j^\alpha\right)\frac{\partial}{\partial r_{ij}^\alpha}\left(\frac{1}{r_{ij}} - w_{qd}\tilde{I}_{s_i s_j}(r_{ij})\right)}^{\text{charge-dipole}} \overbrace{-\kappa\sum_{\alpha,\beta} d_i^\alpha d_j^\beta \frac{\partial^2}{\partial r_{ij}^\beta \partial r_{ij}^\alpha}\left(\frac{1}{r_{ij}} - w_{dd}\tilde{I}_{s_i s_j}(r_{ij})\right)}^{\text{dipole-dipole}},$$

where $\kappa \equiv 1/(4\pi\epsilon_0)$; q_i and d_i^α denote the charge and the αth Cartesian component of the dipole moment, respectively, of ion i; $w_{qq}, w_{qd}, w_{dd} \in \boldsymbol{\eta}$ are parameters that we fit; and the function $\tilde{I}_{s_i s_j}$ is a correction to $1/r_{ij}$ that accounts for overlap between the electron clouds of ions i and j [51,52]. Its mathematical form is

$$\tilde{I}_{s_i s_j}(r_{ij}) \equiv c_{s_i s_j} e^{-b_{s_i s_j} r_{ij}} \left[\sum_{k=0}^{n_k+1} \frac{(b_{s_i s_j} r_{ij})^k}{k!} - \frac{b_{s_i s_j}}{n_k+1} \sum_{k=0}^{n_k} \frac{(b_{s_i s_j} r_{ij})^k}{k!} \right],$$

where $n_k = 4$, and $b_{ss'}, c_{ss'} \in \boldsymbol{\eta}$ are parameters that we fit [51,52].

Polarizable ions with variable charges

What follows is a description of the form of our variable charge and polarizable ion force field, which we used to validate the results of simulations with our fixed charge polarizable ion force field. The fixed charge force field is a special case of the variable charge force field, which can be viewed as its $A_{s_i} \to \infty$ and $B_{s_i} \to \infty$ limit. Alternatively, it can be viewed as the variable charge force field when, for each ion i, parameters A_{s_i} and B_{s_i} are zero and Δq_i has a fixed value of zero.

The charge of ion i is $q_i \equiv q^0_{s_i} + \Delta q_i$, where $q^0_{s_i} \in \boldsymbol{\eta}$ is a parameter that we fit. The values of Δq_i and $\mathbf{d}_i \equiv (d_i^1, d_i^2, d_i^3)$ change as ions move because their values are those that minimize the sum, $U^{\text{elect}} + U^{\text{self}}$, of the electrostatic interactions and the ions' self-energies under the constraint $\sum_i \Delta q_i = 0$. The self-energy, $U_i^{\text{self}}(\Delta q_i, \mathbf{d}_i)$, is the energy cost of deforming its spherically symmetric electron cloud to give it a dipole moment $\mathbf{d}_i$, and of changing its charge by Δq_i relative to the reference charge, $q^0_{s_i}$.

We express the self-energy of ion i as a Taylor expansion about its reference state, $(\Delta q_i, \mathbf{d}_i) = (0, 0)$, as follows:

$$\begin{aligned} U_i^{\text{self}} &= U_i^0 + \left.\frac{\partial U_i^{\text{self}}}{\partial(\Delta q_i)}\right|_{(0,0)} \Delta q_i + \left.\frac{\partial U_i^{\text{self}}}{\partial(d_i^\alpha)}\right|_{(0,0)} d_i^\alpha \\ &\quad + \frac{1}{2}\left.\frac{\partial^2 U_i^{\text{self}}}{\partial(\Delta q_i)^2}\right|_{(0,0)} \Delta q_i^2 + \sum_{\alpha,\beta} \frac{1}{2}\left.\frac{\partial^2 U_i^{\text{self}}}{\partial d_i^\alpha \partial d_i^\beta}\right|_{(0,0)} d_i^\alpha d_i^\beta \\ &\quad + \sum_\alpha \frac{1}{2}\left.\frac{\partial^2 U_i^{\text{self}}}{\partial(\Delta q_i)\partial d_i^\alpha}\right|_{(0,0)} \Delta q_i d_i^\alpha + \cdots \\ &= A_{s_i}\Delta q_i + B_{s_i}\Delta q_i^2 + \sum_\alpha C_{s_i}(d_i^\alpha)^2, \end{aligned}$$

where the three terms that are linear in d_i^α vanish by symmetry and $A_{s_i}, B_{s_i}, C_{s_i} \in \boldsymbol{\eta}$ are parameters that we fit.

Note that the isotropic polarizability of species s_i is $\alpha_{s_i} \equiv 1/(2C_{s_i})$, and that, if ions did not overlap, minimizing $U^{\text{elect}} + U^{\text{self}}$ with respect to the sets $\{\Delta q_i\}$ and $\{\mathbf{d}_i\}$ would ensure that the dipole moment of ion i was $\mathbf{d}_i = \alpha_{s_i}\mathbf{E}_i$, where $\mathbf{E}_i$ is the electric field at the position $\mathbf{r}_i$ of ion i from the charges and dipole moments of all other ions. Therefore, at each time step of our MD simulations, the sets $\{\Delta q_i\}$ and $\{\mathbf{d}_i\}$ that minimize $U^{\text{elect}} + U^{\text{self}}$ provide a simplified description of either the ground state, or the photoexcited stationary state, of the electrons at that time step's set of atomic positions.

In our simulations we found the sets $\{\Delta q_i\}$ and $\{\mathbf{d}_i\}$ at each time step by iterating them to self-consistency, but they can also be found by direction minimization, matrix inversion, or a combination of all three approaches [51,52,57]. *Extended Lagrangian* methods of evolving sets of induced dipole moments or variable charges have also been proposed [78–80]. However, the so-called *fictitious mass* parameters on which extended Lagrangian methods depend can influence forces significantly, unphysically, and unpredictably [54,81,82].

APPENDIX B: INFRARED ABSORPTION SPECTRUM

We now derive an expression for the infrared absorption coefficient by expressing the infrared absorption intensity in terms of the quantum mechanical autocorrelation of the polarization $\mathbf{P}$ using perturbation theory. First we derive the transition probability from state $|i\rangle$ to state $|f\rangle$ per unit time using *Fermi's golden rule*, to the first order of perturbation, which is

$$P_{i\to f} = \frac{2\pi}{\hbar}|\langle f|\Delta\mathcal{H}|i\rangle|^2\rho(E_f), \tag{B1}$$

where $\Delta\mathcal{H}$ is the perturbing Hamiltonian, $\rho(E_f)$ is the density of states at the energy E_f of the final states, $|i\rangle$ and $|f\rangle$ are the initial and final state, respectively. Consider a monochromatic electric field of frequency ω,

$$\mathbf{E}_\omega = |\mathbf{E}_\omega|\cos(\omega t)\hat{\varepsilon}$$

where $\hat{\varepsilon}$ is the unit vector along the electric field and $|\mathbf{E}_\omega|$ is the amplitude of the field. The interaction between the field and the system perturbs the Hamiltonian by

$$\Delta\mathcal{H} = -\mathbf{P}\cdot\mathbf{E}_\omega,$$

where $\mathbf{P}$ is the total polarization operator. Equation (B1) then becomes

$$P_{i\to f}(\omega) = \frac{\pi|\mathbf{E}_\omega|^2}{2\hbar^2}|\langle f|\hat{\varepsilon}\cdot\mathbf{P}|i\rangle|^2[\delta(\omega_{fi}-\omega)+\delta(\omega_{fi}+\omega)],$$

where $\omega_{fi} = \omega_f - \omega_i$. Then, the rate of energy loss from the radiation to the material can be written as

$$\begin{aligned} -\dot{\mathbf{E}}_{\text{rad}} &= \sum_i\sum_f \rho_i\hbar\omega_{fi}P_{i\to f} \\ &= \frac{\pi|\mathbf{E}_\omega|^2}{2\hbar}\sum_{f,i}\omega_{fi}(\rho_i-\rho_f)|\langle f|\hat{\varepsilon}\cdot\mathbf{P}|i\rangle|^2\delta(\omega_{fi}-\omega) \\ &= \frac{\pi|\mathbf{E}_\omega|^2}{2\hbar}(1-e^{-\beta\hbar\omega})\omega\sum_{f,i}\rho_i|\langle f|\hat{\varepsilon}\cdot\mathbf{P}|i\rangle|^2\delta(\omega_{fi}-\omega), \end{aligned}$$

where ρ_i is the probability of initially being in state i, of an thermal equilibrated initial system as

$$\rho_f = \rho_i e^{-\beta\hbar\omega_{\rho i}},$$

$$\rho_i - \rho_f = \rho_i(1-e^{-\beta\hbar\omega_{fi}}).$$

By dividing the average incident energy flux by the magnitude of the Poynting vector, $|\mathbf{S}| = \frac{cn}{2\mu_0}|\mathbf{E}_\omega|^2$, we obtain an

expression for the absorption coefficient:

$$\alpha(\omega) = \frac{\mu_0 \pi}{\hbar c n}(1 - e^{-\beta\hbar\omega})\omega \sum_{f,i} \rho_i |\langle f|\hat{\varepsilon}\cdot\mathbf{P}|i\rangle|^2 \delta(\omega_{fi} - \omega)$$
$$= A(1 - e^{-\beta h\omega})\omega \int_{-\infty}^{\infty} dt e^{-i\omega t}\langle \mathbf{P}(t)\cdot\mathbf{P}(0)\rangle, \qquad \text{(B2)}$$

where A is a constant, and the refractive index, n, is assumed to be approximately independent of ω. This is a quasiclassical expression that incorporates quantum mechanical ω-dependent prefactors into the classical correlation function. In the expression for the absorption coefficient shown above, we have replaced $\langle \hat{\varepsilon}\cdot\mathbf{P}(t)\ \hat{\varepsilon}\cdot\mathbf{P}(0)\rangle$ with $\langle \mathbf{P}(t)\ \mathbf{P}(0)\rangle$. This assumption is valid either when the field is parallel to the total polarization density ($\mathbf{E}_\omega \parallel \mathbf{P}$), or when the sample is polycrystalline, consisting of many domains with different orientations.

Calculating infrared spectra in MD simulations

To calculate $\alpha(\omega)$ from an MD simulation one must be able to calculate variations of $\mathbf{P}$. Although it is well known that $\mathbf{P}$ is ill defined, the variation of $\mathbf{P}$ in an insulator, which is a polarization current density $\mathbf{J}$, is well defined [83,84]. However, under the periodic boundary conditions that we used in our simulations, $\mathbf{J}$ is only well defined if the contribution to it from charge that crosses a boundary can be calculated. This means that when a charge traveling in direction $\hat{u}$ crosses a boundary that is normal to $\hat{u}$, it is not moved to the opposite boundary. Moving it to the opposite boundary would change its contribution to $\mathbf{J}$ from a small contribution in direction $\hat{u}$ to a much larger contribution in direction $-\hat{u}$, which is inversely proportional to the time step.

Therefore, in MD simulations with our fixed charge force field, we used the definition

$$\mathbf{P} \equiv \frac{1}{\Omega}\sum_i (q_i \mathbf{r}_i + \mathbf{d}_i),$$

where Ω is the simulation cell's volume. Under this definition, variations of $\mathbf{P}$ are well defined as long as ions' positions change continuously. Since we simulated under periodic boundary conditions, this meant that when ion i crossed one of the simulation cell's boundaries it remained where it was, rather than being shifted by a simulation cell lattice vector, $\mathbf{A}$, to the opposite boundary. Moving it to the opposite boundary would change $\mathbf{P}$ discontinuously by $q_i\mathbf{A}/\Omega$.

It was not possible to calculate infrared spectra using our variable charge force field for the following reason. The ions' charges vary continuously and, when an ion's charge increases, the origin of its increased charge is not defined, which means that the current that transported charge to it is not defined. The change of each ion's charge cannot be said to come from any particular ion unless only two ions' charges change. However, even in that case, the periodic boundary conditions would mean that the direction of the current that transported charge between the ions would not be defined.

[1] S. Fahy and R. Merlin, Reversal of ferroelectric domains by ultrashort optical pulses, Phys. Rev. Lett. **73**, 1122 (1994).

[2] M. W. Wefers, H. Kawashima, and K. A. Nelson, Optical control over femtosecond polarization dynamics, J. Phys. Chem. Solids **57**, 1425 (1996).

[3] T. Qi, Y.-H. Shin, K.-L. Yeh, K. A. Nelson, and A. M. Rappe, Collective coherent control: Synchronization of polarization in ferroelectric $PbTiO_3$ by shaped THz fields, Phys. Rev. Lett. **102**, 247603 (2009).

[4] A. Subedi, Proposal for ultrafast switching of ferroelectrics using midinfrared pulses, Phys. Rev. B **92**, 214303 (2015).

[5] F. Chen, Y. Zhu, S. Liu, Y. Qi, H. Y. Hwang, N. C. Brandt, J. Lu, F. Quirin, H. Enquist, P. Zalden, T. Hu, J. Goodfellow, M.-J. Sher, M. C. Hoffmann, D. Zhu, H. Lemke, J. Glownia, M. Chollet, A. R. Damodaran, J. Park *et al.*, Ultrafast terahertz-field-driven ionic response in ferroelectric $BaTiO_3$, Phys. Rev. B **94**, 180104 (2016).

[6] R. Mankowsky, A. von Hoegen, M. Först, and A. Cavalleri, Ultrafast reversal of the ferroelectric polarization, Phys. Rev. Lett. **118**, 197601 (2017).

[7] H. Akamatsu, Y. Yuan, V. A. Stoica, G. Stone, T. Yang, Z. Hong, S. Lei, Y. Zhu, R. C. Haislmaier, J. W. Freeland, L.-Q. Chen, H. Wen, and V. Gopalan, Light-activated gigahertz ferroelectric domain dynamics, Phys. Rev. Lett. **120**, 096101 (2018).

[8] F. Rubio-Marcos, D. A. Ochoa, A. Del Campo, M. A. Garcia, G. R. Castro, J. F. Fernandez, and J. E. Garcia, Reversible optical control of macroscopic polarization in ferroelectrics, Nat. Photon. **12**, 29 (2018).

[9] T. Li, A. Lipatov, H. Lu, H. Lee, J.-W. Lee, E. Torun, L. Wirtz, C.-B. Eom, J. Íñiguez, A. Sinitskii, and A. Gruverman, Optical control of polarization in ferroelectric heterostructures, Nat. Commun. **9**, 3344 (2018).

[10] V. I. Yukalov and E. P. Yukalova, Ultrafast polarization switching in ferroelectrics, Phys. Rev. Res. **1**, 033136 (2019).

[11] A. V. Kimel, A. M. Kalashnikova, A. Pogrebna, and A. K. Zvezdin, Fundamentals and perspectives of ultrafast photoferroic recording, Phys. Rep. **852**, 1 (2020).

[12] A. Bagri, A. Jana, G. Panchal, D. M. Phase, and R. J. Choudhary, Amalgamation of photostriction, photodomain, and photopolarization effects in $BaTiO_3$ and its electronic origin, ACS Appl. Electron. Mater. **4**, 4438 (2022).

[13] P. Chen, C. Paillard, H. J. Zhao, J. Iniguez, and L. Bellaiche, Deterministic control of ferroelectric polarization by ultrafast laser pulses, Nat. Commun. **13**, 2566 (2022).

[14] L. Gao, C. Paillard, and L. Bellaiche, Photoinduced control of ferroelectricity in hybrid-improper ferroelectric superlattices, Phys. Rev. B **107**, 104109 (2023).

[15] F. Rubio-Marcos, A. Del Campo, P. Marchet, and J. F. Fernández, Ferroelectric domain wall motion induced by polarized light, Nat. Commun. **6**, 6594 (2015).

[16] D. Paez-Margarit, F. Rubio-Marcos, D. A. Ochoa, A. Del Campo, J. F. Fernandez, and J. E. Garcia, Light-induced capacitance tunability in ferroelectric crystals, ACS Appl. Mater. Interfaces **10**, 21804 (2018).

[17] C. J. Brennan and K. A. Nelson, Direct time-resolved measurement of anharmonic lattice vibrations in ferroelectric crystals, J. Chem. Phys. **107**, 9691 (1997).

[18] A. Cavalleri, S. Wall, C. Simpson, E. Statz, D. W. Ward, K. A. Nelson, M. Rini, and R. W. Schoenlein, Tracking the motion of charges in a terahertz light field by femtosecond X-ray diffraction, Nature (London) **442**, 664 (2006).

[19] K. Istomin, V. Kotaidis, A. Plech, and Q. Kong, Dynamics of the laser-induced ferroelectric excitation in $BaTiO_3$ studied by x-ray diffraction, Appl. Phys. Lett. **90**, 022905 (2007).

[20] D. S. Rana, I. Kawayama, K. Mavani, K. Takahashi, H. Murakami, and M. Tonouchi, Understanding the nature of ultrafast polarization dynamics of ferroelectric memory in the multiferroic $BiFeO_3$, Adv. Mater. **21**, 2881 (2009).

[21] G. P. Wiederrecht, T. P. Dougherty, L. Dhar, K. A. Nelson, A. M. Weiner, and D. E. Leaird, Femtosecond impulsive stimulated Raman scattering studies of $LiTaO_3$, Ferroelectrics **144**, 1 (1993).

[22] H. J. Zeiger, J. Vidal, T. K. Cheng, E. P. Ippen, G. Dresselhaus, and M. S. Dresselhaus, Theory for displacive excitation of coherent phonons, Phys. Rev. B **45**, 768 (1992).

[23] S. Hunsche, K. Wienecke, T. Dekorsy, and H. Kurz, Impulsive softening of coherent phonons in tellurium, Phys. Rev. Lett. **75**, 1815 (1995).

[24] P. Tangney and S. Fahy, Calculations of the A_1 phonon frequency in photoexcited tellurium, Phys. Rev. Lett. **82**, 4340 (1999).

[25] M. Bargheer, N. Zhavoronkov, Y. Gritsai, J. Woo, D. Kim, M. Wörner, and T. Elsässer, Coherent atomic motions in a nanostructure studied by femtosecond X-ray diffraction, Science **306**, 1771 (2004).

[26] É. D. Murray, D. M. Fritz, J. K. Wahlstrand, S. Fahy, and D. A. Reis, Effect of lattice anharmonicity on high-amplitude phonon dynamics in photoexcited bismuth, Phys. Rev. B **72**, 060301(R) (2005).

[27] P. Tangney and S. Fahy, Density-functional theory approach to ultrafast laser excitation of semiconductors: Application to the A_1 phonon in tellurium, Phys. Rev. B **65**, 054302 (2002).

[28] F. Gu, E. Murray, and P. Tangney, Carrier-mediated control over the soft mode and ferroelectricity in $BaTiO_3$, Phys. Rev. Mater. **5**, 034414 (2021).

[29] F. Gu, J. Wang, Z.-J. Lang, and W. Ku, Quantum fluctuation of ferroelectric order in polar metals, npj Quantum Mater. **8**, 49 (2023).

[30] S. Acharya, S. Chouthe, H. Graener, T. Böntgen, C. Sturm, R. Schmidt-Grund, M. Grundmann, and G. Seifert, Ultrafast dynamics of the dielectric functions of ZnO and $BaTiO_3$ thin films after intense femtosecond laser excitation, J. Appl. Phys. **115**, 053508 (2014).

[31] E. S. Zijlstra, L. L. Tatarinova, and M. E. Garcia, Laser-induced phonon-phonon interactions in bismuth, Phys. Rev. B **74**, 220301(R) (2006).

[32] E. D. Murray, S. Fahy, D. Prendergast, T. Ogitsu, D. M. Fritz, and D. A. Reis, Phonon dispersion relations and softening in photoexcited bismuth from first principles, Phys. Rev. B **75**, 184301 (2007).

[33] D. M. Fritz, D. A. Reis, B. Adams, R. A. Akre, J. Arthur, C. Blome, P. H. Bucksbaum, A. L. Cavalieri, S. Engemann, S. Fahy, R. W. Falcone, P. H. Fuoss, K. J. Gaffney, M. J. George, J. Hajdu, M. P. Hertlein, P. B. Hillyard, M. H.-V. Hoegen, M. Kammler, J. Kaspar *et al.*, Ultrafast bond softening in bismuth: Mapping a solid's interatomic potential with X-rays, Science **315**, 633 (2007).

[34] S. K. Sundaram and E. Mazur, Inducing and probing non-thermal transitions in semiconductors using femtosecond laser pulses, Nat. Mater. **1**, 217 (2002).

[35] E. Gamaly, The physics of ultra-short laser interaction with solids at non-relativistic intensities, Phys. Rep. **508**, 91 (2011).

[36] J. Shah, *Ultrafast Spectroscopy of Semiconductors and Semiconductor Nanostructures*, 2nd ed., Springer Series in Solid-State Sciences (Springer Berlin, Heidelberg, 1999).

[37] K. C. Phillips, H. H. Gandhi, E. Mazur, and S. K. Sundaram, Ultrafast laser processing of materials: A review, Adv. Opt. Photon. **7**, 684 (2015).

[38] C. A. D. Roeser and E. Mazur, Light-matter interactions on the femtosecond time scale, in *Frontiers of Optical Spectroscopy*, edited by B. Di Bartolo and O. Forte (Springer Netherlands, Dordrecht, 2005), pp. 29–54.

[39] A. V. Kuznetsov and C. J. Stanton, Theory of coherent phonon oscillations in semiconductors, Phys. Rev. Lett. **73**, 3243 (1994).

[40] F. Caruso and M. Zacharias, Quantum theory of light-driven coherent lattice dynamics, Phys. Rev. B **107**, 054102 (2023).

[41] J. D. Axe, Apparent ionic charges and vibrational eigenmodes of $BaTiO_3$ and other perovskites, Phys. Rev. **157**, 429 (1967).

[42] J. T. Last, Infrared-absorption studies on barium titanate and related materials, Phys. Rev. **105**, 1740 (1957).

[43] J. C. Slater, The Lorentz correction in barium titanate, Phys. Rev. **78**, 748 (1950).

[44] G. Coiana, J. Lischner, and P. Tangney, Breakdown of phonon band theory in MgO, Phys. Rev. B **109**, 014310 (2024).

[45] J. Fallon, Multiscale theory and simulation of barium titanate, Ph.D. thesis, Imperial College London, 2014.

[46] G. Coiana, Imaging the breakdown of phonon quasiparticle theory in MgO and $BaTiO_3$ with atomistic simulations, Ph.D. thesis, Imperial College London, 2023.

[47] J. P. Perdew, A. Ruzsinszky, G. I. Csonka, O. A. Vydrov, G. E. Scuseria, L. A. Constantin, X. Zhou, and K. Burke, Restoring the density-gradient expansion for exchange in solids and surfaces, Phys. Rev. Lett. **100**, 136406 (2008).

[48] P. M. Morse, Diatomic molecules according to the wave mechanics. II. Vibrational levels, Phys. Rev. **34**, 57 (1929).

[49] R. E. Cohen, Origin of ferroelectricity in perovskite oxides, Nature (London) **358**, 136 (1992).

[50] R. E. Cohen and H. Krakauer, Lattice dynamics and origin of ferroelectricity in $BaTiO_3$: Linearized-augmented-plane-wave total-energy calculations, Phys. Rev. B **42**, 6416 (1990).

[51] J. Sarsam, Development and application of atomistic force fields for ionic materials, Ph.D. thesis, Imperial College London, 2013.

[52] V. Nemytov, Towards an accurate and transferable charge transfer model in polarisable interatomic potentials, Ph.D. thesis, Imperial College London, 2018.

[53] P. Tangney and S. Scandolo, An *ab initio* parametrized interatomic force field for silica, J. Chem. Phys. **117**, 8898 (2002).

[54] P. Tangney and S. Scandolo, A many-body interatomic potential for ionic systems: Application to MgO, J. Chem. Phys. **119**, 9673 (2003).

[55] J. Sarsam, M. W. Finnis, and P. Tangney, Atomistic force field for alumina fit to density functional theory, J. Chem. Phys. **139**, 204704 (2013).

[56] X. J. Han, L. Bergqvist, P. H. Dederichs, H. Müller-Krumbhaar, J. K. Christie, S. Scandolo, and P. Tangney, Polarizable interatomic force field for TiO_2 parametrized using density functional theory, Phys. Rev. B **81**, 134108 (2010).

[57] A. K. Rappé and W. A. Goddard III, Charge equilibration for molecular dynamics simulations, J. Phys. Chem. **95**, 3358 (1991).

[58] See Supplemental Material at http://link.aps.org/supplemental/10.1103/PhysRevB.110.014307 for the force field parameters and some tests of the force fields' accuracies, which includes Refs. [59–63].

[59] G. H. Kwei, A. C. Lawson, S. J. L. Billinge, and S. W. Cheong, Structures of the ferroelectric phases of barium titanate, J. Phys. Chem. **97**, 2368 (1993).

[60] S. Tinte, M. G. Stachiotti, M. Sepliarsky, R. L. Migoni, and C. O. Rodriguez, Atomistic modelling of $BaTiO_3$ based on first-principles calculations, J. Phys.: Condens. Matter **11**, 9679 (1999).

[61] R. D. King-Smith and D. Vanderbilt, First-principles investigation of ferroelectricity in perovskite compounds, Phys. Rev. B **49**, 5828 (1994).

[62] F. D. Murnaghan, The compressibility of media under extreme pressures, Proc. Natl. Acad. Sci. USA **30**, 244 (1944).

[63] A. Togo and I. Tanaka, First principles phonon calculations in materials science, Scr. Mater. **108**, 1 (2015).

[64] F. Gu, Controlling structural change in $BaTiO_3$ by ultrafast laser excitation, Ph.D. thesis, Imperial College London, 2021.

[65] P. Tangney, Improving molecular dynamics simulations of simple ionic systems, Ph.D. thesis, SISSA, Trieste, 2002.

[66] L.-P. Wang and T. Van Voorhis, Communication: Hybrid ensembles for improved force matching, J. Chem. Phys. **133**, 231101 (2010).

[67] V. M. Goldschmidt, Die gesetze der krystallochemie, Naturewissenschaften **14**, 477 (1926).

[68] W. Zhong, D. Vanderbilt, and K. M. Rabe, Phase transitions in $BaTiO_3$ from first principles, Phys. Rev. Lett. **73**, 1861 (1994).

[69] J. Hlinka, T. Ostapchuk, D. Nuzhnyy, J. Petzelt, P. Kuzel, C. Kadlec, P. Vanek, I. Ponomareva, and L. Bellaiche, Coexistence of the phonon and relaxation soft modes in the terahertz dielectric response of tetragonal $BaTiO_3$, Phys. Rev. Lett. **101**, 167402 (2008).

[70] J. Weerasinghe, L. Bellaiche, T. Ostapchuk, P. Kužel, C. Kadlec, S. Lisenkov, I. Ponomareva, and J. Hlinka, Emergence of central mode in the paraelectric phase of ferroelectric perovskites, MRS Commun. **3**, 41 (2013).

[71] R. Pirc and R. Blinc, Off-center Ti model of barium titanate, Phys. Rev. B **70**, 134107 (2004).

[72] M. S. Senn, D. A. Keen, T. C. A. Lucas, J. A. Hriljac, and A. L. Goodwin, Emergence of long-range order in $BaTiO_3$ from local symmetry-breaking distortions, Phys. Rev. Lett. **116**, 207602 (2016).

[73] L. Gigli, M. Veit, M. Kotiuga, G. Pizzi, N. Marzari, and M. Ceriotti, Thermodynamics and dielectric response of $BaTiO_3$ by data-driven modeling, npj Comput. Mater. **8**, 209 (2022).

[74] I. B. Bersuker, On the origin of ferroelectricity in perovskite-type crystals, Phys. Lett. **20**, 589 (1966).

[75] R. Comes, M. Lambert, and A. Guinier, The chain structure of $BaTiO_3$ and $KNbO_3$, Solid State Commun. **6**, 715 (1968).

[76] A. S. Chaves, F. C. S. Barreto, R. A. Nogueira, and B. Zēks, Thermodynamics of an eight-site order-disorder model for ferroelectrics, Phys. Rev. B **13**, 207 (1976).

[77] P. Gayathri, M. J. Swamynathan, M. Shaikh, A. Ghosh, and S. Ghosh, Switching of hybrid improper ferroelectricity in oxide double perovskites, Chem. Mater. **35**, 6612 (2023).

[78] M. Sprik and M. L. Klein, A polarizable model for water using distributed charge sites, J. Chem. Phys. **89**, 7556 (1988).

[79] M. Sprik, Computer simulation of the dynamics of induced polarization fluctuations in water, J. Phys. Chem. **95**, 2283 (1991).

[80] K. Nomura, P. E. Small, R. K. Kalia, A. Nakano, and P. Vashishta, An extended-Lagrangian scheme for charge equilibration in reactive molecular dynamics simulations, Comput. Phys. Commun. **192**, 91 (2015).

[81] P. Tangney and S. Scandolo, How well do Car–Parrinello simulations reproduce the Born–Oppenheimer surface? Theory and examples, J. Chem. Phys. **116**, 14 (2002).

[82] P. Tangney, On the theory underlying the Car-Parrinello method and the role of the fictitious mass parameter, J. Chem. Phys. **124**, 044111 (2006).

[83] R. Resta and D. Vanderbilt, Theory of polarization: A modern approach, in *Physics of Ferroelectrics*, Topics in Applied Physics (Springer, Berlin, Heidelberg, 2007), Vol. 105, pp. 31–68.

[84] P. Tangney, Electricity at the macroscale and its microscopic origins, arXiv:2403.13981 [cond-mat.mtrl-sci].